Progressive Collapse Resistance of Two-Storey Seismic Configured Steel Sub-Frames Using Welded Connections

Kai Qian[1]*, Xi Lan[1], Zhi Li[1], Yi Li[2], Feng Fu[3]

[1]College of Civil Engineering and Architecture, Guangxi University, Nanning, China, 530004.

[2] Key Lab. of Urban Security and Disaster Engineering of Ministry of Education, Beijing University of Technology, Beijing 1000124, China

[3] School of Mathematics, Computer Science and Engineering, City, University of London, London, EC1V 0HB UK.

Abstract:

This paper presents the experimental and numerical investigation on resistance of two-storey steel sub-frames subjected to a middle column removal scenario. Two different types of 1/2 scaled steel sub-frames with seismic configuration were fabricated and tested, they are: (1) welded connections with gross beam section (GBS) and (2) welded connections with reduced beam section (RBS, typically used for energy dissipation in earthquake design). Based on the test results, finite element models using explicit software LS-DYNA which can accurately replicate the response of the frames were created and validated. Using the validated model, the parametric studies were also performed to investigate the effect of different parameters on the progressive collapse resistance of the frame. Base on the experimental and numerical studies, the failure mechanism and collapse resistance capacities of these two types of frame systems are first time investigated. The test results indicated that the welded connections with RBS exhibits better performance due to the guaranteed formation of plastic hinges at the location of reduced section, as well as the avoidance of welding heat effect and brittle weld fracture at beam to column connections. Thus, RBS exhibits larger deformation capacity which is favorable in mitigating the possible progressive collapse.

Keywords: Experimental; Numerical; Multi-Storey; Progressive Collapse; Steel; Weld Connection

* Corresponding author. Tel.: 86+771-3232894, E-mail address: qiankai@gxu.edu.cn

1. Introduction

Progressive collapse refers to a situation in which the failure of a local failure causes a major collapse, with the magnitude being disproportionate to the initial event. In recent years, the increasing terrorist attacks have increased the likelihood of progressive collapse. Due to its catastrophic consequences, progressive collapse has been the focus of engineers and researchers in the civil engineering research community.

Progressive collapse is a dynamic event, and many studies have examined the dynamic collapse performance. Previous studies have introduced the strain rate effects in dynamic progressive collapse analysis [1-2]. It has been reported that the strain rate effects could change the failure mechanism of the connections and influence the capacity of progressive collapse. To approximately compensate for dynamic effects when a static procedure is used, many procedures and explicit expressions have been proposed [3-5] and dynamic increase factor was investigated [6-8]. Ferraioli [9] developed a modal pushdown analysis procedure for progressive collapse assessment of multi-storey steel frame buildings under sudden removal scenario of a column due to catastrophic events. For steel frames, catenary action (CA) is an essential load resisting mechanism to redistribute the loads after column removal [10-11].

However, more researchers use static procedure during the test due to the difficulty in performing the dynamic tests. Some of existing tests are relied on two-dimensional tests replicate whole beam span and portions of structural frame were designed as boundary conditions [12-15]. Lew et al. [12] conducted an experimental study of two steel moment frame under a column-removal scenario, to investigate the behavior and failure modes of steel joints including the development of catenary action. Majority of these test specimens were only half beam span and the extremity of connections was pinned which was a simplified boundary condition [16-20]. Yang and Tan [16] presented seven experimental tests on the performance of common types of bolted steel beam-column joints under a central-column-removal scenario subjected to catenary action, and it indicated that tensile capacities of beam-column joints after undergoing large rotations usually control the failure mode and the formation of catenary action. Li et al. [17] investigated behavior of two steel joints subjected to column loss and effective catenary action was developed in both specimens. The effects of slab flange were also considered [21-28].

Although several studies had been carried out on progressive collapse resistance of steel sub-assemblages with different types of connections, studies especially tests on multi-story beam-column sub-frames were still scarce. Li et al. [29-30] carried out a series test of two-bay by two-story steel frame with welded connections subjected to sudden column removal scenario. It was found that the mobilization of catenary action in the first story was more significant than that of second story. Thus, assuming all upper stories above the lost column performed similarly and developing equally load resistance may be not accurate. It was necessary to carry out multi-story frame tests for deep understanding the behavior of steel frames subjected to the loss of column scenarios. To tackle this problem, in this paper, a series of two two-story by two-bay half-scale steel sub-frames using welded connections with seismic configuration were fabricated and tested. In this study, a quasi-static loading scheme is adopted and strain rate effects are not considered. Based on the test results, finite element models using explicit software LS-DYNA which can accurately replicate the response of the frames are created and validated. Using the validated model, the parametric studies are also performed to investigate the effect of different parameters on the progressive collapse resistance of the frame.

2. Experimental program

2.1. Test specimens

As shown in Fig. 1, the prototype frame was a six-story steel frame with six bays in both longitudinal and transverse directions. The span in longitudinal and transverse directions was 8.4 m and 6.0 m, respectively. The specimen was designed in accordance with seismic design requirements of AISC-341 [31]. The design dead and live loads were 5.1 kN/m^2 and 3.0 kN/m^2, respectively. The connections were designed in accordance to FEMA 350 [32]. Only two-bay by two-story sub-frame was extracted from the prototype frame for experimental tests for a middle column lost. Owing to space, facility and cost limitation, only half-scale specimens were tested. As represented in Fig. 2, the beam span was 3000 mm and column height was 1500 mm. Extra overhanging beam with length of 655 mm, connected with a roller, was extended outside the side column to simulate horizontal constraints from the remaining structures of the six-story steel frame. Two types of connections are tested: (1) welded connection with gross beam section (Specimen GBS) and welded connection with reduced beam section RBS (Specimen RBS), as it shown in Fig. 3. For GBS, the beam flange and web were welded to column flange by full penetration welds. Continuity plates with thickness of 10 mm were used in the column. For RBS, similar to GBS, the beam flanges and web were connected to the column by same weld. However, partial of beam flanges, at a distance of 70 mm from the column flange, was cut in a circular manner, as shown in Fig. 3b.

In both specimens, HW 150×150×7×10 and HN 200×100×5.5×8 were used for column and beam, respectively. The steel used in test was Chinese Q235. The yield strength (f_y), yield strain (μ_y), tensile strength (f_u), fracture strength (f_f), and total elongation (A_{gt}) of the steel in different components are given in Table1.

2.2. Test setup and instrumentation

Fig. 4 gives the experimental setup and locations of instrumentations. The bottom of the side column was connected to a pin support while the overhanging beam at both sides was connected to an A-frame via a roller connection. The middle column at first story was removed prior to loading process started. This is to simulate column removal due to accidental or incidental events. A hydraulic jack (Item 1 in Fig. 4) was utilized to apply the vertical displacement at the top of middle column until complete failure. A steel column together with a steel assembly was installed beneath the hydraulic jack (Item 1 in Fig. 4) to prevent any undesired out-of-plane failure. The axial compressive force with ratio of 0.3 to it is capacity was applied at the side column by a hydraulic jack (Item 4 in Fig. 4) with a self-equilibrium system. To monitor the structural behavior, extensive instrumentations were installed. A load cell (Item 2 in Fig. 4) was installed below the hydraulic jack (Item 1 in Fig. 4) to measure the applied concentrated load. Tension/compression load cell (Item 5 in Fig. 4) was installed at each roller connection to measure the horizontal reaction force of the roller.

To measure the vertical and horizontal reaction forces of the pin support, a load pin (Item 6 in Fig. 4) was installed at each pin support. Moreover, a series of linear variable differential transformers (LVDTs) (Item 7 in Fig. 4) were installed along the beam span and column height to measure the deformation shape of the beams and columns.

As shown in Fig. 2, 12 sections a series of strain gauges or strain rosettes were employed to monitor the axial forces and bending moments of beams in detail. Moreover, the load resistance from each story was also determined based on the strain gauge results.

3. Experimental results

As mentioned above, Specimens GBS and RBS were tested under monotonic vertical load until failure. The test results were described as below, and the key results were summarized in Table 2.

3.1. Load-displacement curves

Fig. 5 shows the vertical load-displacement curve of GBS and RBS. At the initial loading stage, the specimens were in elastic stage, and the vertical force increased more or less linearly with the increase of vertical displacement.

For GBS, the yield load of 147.8 kN was recorded when middle column displacement (MCD) reached 45 mm, which corresponded to the rotation θ of 0.015 rad. The rotation was defined as the ratio of MCD to the beam span. However, yield load of RBS was106.8 kN at an MCD of 37 mm (θ = 0.012 rad). Therefore, the initial stiffness, representing the ratio of yield load to yield displacement, of GBS and RBS was 3.3 kN/mm and 2.9 kN/mm, respectively. As shown in the figure, the load resistance of GBS was higher than that of RBS before GBS reaching its peak load (PL) of 197.5 kN corresponding to an MCD of 200 mm (θ = 0.067 rad). After reaching PL, the load resistance of GBS began to drop slowly due to weld fracture failure noticed near the connection of the middle column in the first story. However, when MCD reached 281 mm (θ = 0.094 rad), the load resisting capacity of GBS began to re-ascend due to axial force developed in the second story (catenary action). The ultimate deformation of GBS was 377 mm (θ = 0.126 rad) and load resisting capacity at ultimate deformation was 187.9 kN, which was about 95.1 % of its PL. Different to GBS, RBS kept increasing until reaching its PL of 407.0 kN at an MCD of 468 mm (θ = 0.156 rad). Thus, the PL and ultimate deformation capacity of RBS was 106.1 % and 24.1 % higher than that of GBS, respectively. The measured rotation capacity of RBS is about 201.0 % of the value determined according to FEMA 350 [32]. Therefore, GBS has a higher initial stiffness and load resisting capacity before the failure. But pre-mature weld failure at beam-column connection would decrease deformation capacity of GBS significantly. For RBS, the plastic hinges were formed at the center of the reduced beam section, which would prevent the early fractures in the welding connection of the specimen.

3.2. Damage development and failure modes

For GBS, with the increase of the vertical displacement, fracture first occurred at the beam flange in the region of middle column on first story (BEMC-1), as well as left beam end close to the edge column on first story (LBESC-1) with MCD recorded of 200 mm (θ = 0.067 rad). Then, the fracture propagates into the web. At an MCD of 377 mm (θ = 0.126 rad) BEMC-1 fractured, while BEMC-2 fractured at the MCD of 410 mm (θ = 0.137 rad). The failure mode of GBS is illustrated in Fig. 6. As shown in the figure, complete fracture was observed in the left side of BEMC-2 and right side of BEMC-1. However, only top flange and partial of web was fractured in LBESC-1.

For RBS, plastic hinges were formed at the reduced sections at an MCD of 37 mm (θ = 0.012 rad). Due to considerable tensile axial force developed in the beams, fracture was first observed at beam reduced section nearby the right side column of first story (RBESC-1) at an MCD of 468 mm (θ = 0.156 rad). Fig. 7 shows the failure mode of RBS. As shown in the figure, fracture only observed in RBESC-1. Further increasing the displacement was prevented due to stroke of the jack reached its capacity. From the figure, the pealing zone of BEMC-1 was greater than that of BEMC-2. And larger plastic rotation was concentrated in BEMC-1.

3.3. Deformation measurements

The deformation shape of edge column was shown in Fig. 8. As shown in Fig. 8a, inward movement was observed at the position coincide with the beam axis. However, the inward movement at the position coincide with the beam axis of second story was much larger than that of first story as greater catenary action developed in there. The pre-mature fracture in BEMC-1 and LBESC-1 prevents further developing catenary action in the beams of first story. Moreover, double curvature was observed in edge column. However, the location of contra-flexural point was varying with increasing MCD. The maximum inward movements of the points coincide with beam axis in the first and second stories were 3.2 mm and 9.1mm, respectively. For RBS, as shown in Fig. 8b, no contra-flexural point was observed in the side column due to both beams developed considerable tensile force. Moreover, the maximum inward movements of the point coincide with beam axis in the first and second stories were 11.6 mm and 21.0 mm, respectively.

Fig. 9 shows the deflection shape of the beams in the first story at different displacement stages. In elastic stage, for both specimens, the deformation shape of the beams was similar to a straight line. For GBS, the beam deformation in the first story was mostly concentrated on the beam end near edge column rather than the middle column, thus the fracture finally developed in BEMC-1. For RBS, further increasing MCD, the deformation of first story appeared on the both beam end nearby the middle column and side column. Plastic hinges formed in reduced beam sections and double curvature was observed.

3.4. Horizontal reaction force

Fig. 10a illustrates the horizontal reaction v.s. vertical displacement curve of GBS. From the figure, compressive force was mainly attributed into the bottom pin support. The maximum compressive force of -24.7 kN was measured at an MCD of 48 mm ($\theta = 0.016$ rad) in the bottom pin support. When the MCD reached 144 mm ($\theta = 0.048$ rad), the compressive force was transferred into tension. However, the tensile force from the bottom pin was always marginal in catenary action stage and majority of tensile force was provided by the rollers connected to the overhanging beams in the first and second stories. However, it should be noted that the maximum tensile force measured in the first and second stories were 126.1 kN and 253.5 kN, respectively. This may due to pre-mature failure occurred at the first story. Focusing on the total reaction force, tensile force was measured when the MCD exceeded 115 mm ($\theta = 0.038$ rad). Thus, for GBS with welded connections, the catenary action was mobilized at 3.8 % of the beam span. Fig. 10b illustrates the horizontal reaction force-vertical displacement curve of RBS. Similarly, the compressive reaction force was mainly attributed into the bottom pin support. However, different to GBS, in catenary action stage, the tensile force from the first and second story was almost identical. The maximum total tensile force was 875.9 kN, which was about 241.0 % of that of GBS.

3.5. Internal force measurements

The axial force and bending moment can be calculated conveniently according to Eqs. 1 and 2. As the middle portion of the beam kept straight during test, strain gauge results in sections B9 and B10 were utilized to determine the internal forces. Fig. 11 is the free body diagram of the beam portion between sections B10 and B9. From basic analysis, the shear force can be calculated by Eq. 3:

$$N_1 = EA\left(\sum_{i=1}^{n} \varepsilon_i\right) \Big/ n \tag{1}$$

$$M_1 = EI\frac{\Delta\varepsilon}{h_w} \tag{2}$$

$$V_1 = \left(M_{B10} - M_{B9}\right) / \Delta L \tag{3}$$

where N_1, M_1 and V_1 are the axial force, bending moment and shear force of sections B9 and B10, respectively; E is the elastic modulus; A is the beam section area; I is the sectional moment of area; $\left(\sum_{i=1}^{n} \varepsilon_i\right) \Big/ n$ is the axial strain of section; $\Delta\varepsilon$ is the difference between the measured strains of three gauges at flanges (an averaged strain for each flange); h_w is the height of web; ΔL is the distance between sections B10 and B9.

The vertical and horizontal force of the beam in the first story could be determined by Eqs. 4 and 5, respectively.

$$F_{V1} = V_1 \cos\theta_{B10} + N_1 \sin\theta_{B10} \tag{4}$$

$$F_{H1} = V_1 \sin\theta_{B10} + N_1 \cos\theta_{B10} \tag{5}$$

where F_{V1} and F_{H1} are the vertical force and horizontal reaction force of a beam in the first story. According to Fig. 9, the deflection between beam spanwise distance of -2250 mm and -750 mm can be approximated as a straight line, θ_{B10} is the rotation at section B10 which equals to the rotation at beam spanwise distance of -2250 mm.

The vertical force and horizontal reaction force of the beam in second story can be calculated similarly. Fig. 12 compares the total vertical load resistance and total horizontal reaction force based on strain gauge results with that measured from tests. As shown in Fig. 12a, for GBS, before MCD reached 280 mm (θ = 0.093 rad), the vertical load resistance and horizontal reaction force determined based on strain gauge results agreed with the load cell measured values well. When MCD was beyond 280 mm (θ = 0.093 rad), the discrepancy became larger due to partial of strain gauges faulted. For RBS, both vertical load resistance and horizontal reaction force determined from strain gauge results agreed with the load cell measured results well. Therefore, it was reliable to use strain gauge results to determine the bending moment and axial force of the beams. Moreover, based on strain gauge results, the load resistance of each story could be determined.

Fig. 13 illustrates the variation of the total bending moment and total axial force of the specimens while Fig. 14 gives the de-composition of load resistance from catenary action (CA) and flexural action (FA). As shown in Fig. 13, before MCD reached 128 mm (θ = 0.043 rad) and 144 mm (θ = 0.048 rad), bending moment and flexural action dominated the load resistance of GBS and RBS, respectively. After that stage, FA and CA worked together to help redistribute the applied load. Thus, it was not accurate to assume that the load resistance purely relied on CA in large deformation stage [33-35].

4. Discussion of experimental results

4.1. Contribution of load resistance

Fig. 15 decomposes the load resistance from first and second stories. It can be seen that the load resistance from the first story dropped quickly after weld fracture at the connection. Therefore, the behavior of each story may be quite different due to variation of quality welding workmanship. For

RBS, the load resistance from each story was similar during the test. However, for both specimens, the load resistance from the first story was slightly larger than that from the second story, similar phenomena has been discovered by Fu [36]. To reveal the difference, the axial force and bending moment results of each story were determined and presented in Fig. 16. As shown in the figure, the bending moment from the first story was slightly larger than that from the second story mainly due to higher rotational restraints from the side column. The axial force in the first story was always tensile during the test while compressive force was measured in the second story first. This could be explained as the two-story frame could be analyzed as a deep beam. The beams in the first story suffered tensile force while the second story suffered compressive force when a concentrated load was initially applied in the middle column.

4.2. Bending moment-axial force interaction diagram

Fig. 17 shows the moment and axial force interaction diagram of tested specimens. The theoretical interaction diagrams of the beam section were calculated based on the measured yield and ultimate strength from coupon tests (ANSI/AISC 360-10 [37]). As shown in the figure, the bending moment capacity of GBS exceeded its theoretical yield capacity. However, it is less than its theoretical ultimate strength. For RBS, the measured bending moment capacity is larger than its theoretical ultimate strength based on reduced section. However, it is still less than the theoretical ultimate strength of GBS.

4.3. Practical implications from experimental results of RBS

The RBS connection was designed to only resist pure bending in seismic loading according to FEMA 350 [32] and ANSI/AISC 358-10 [38]. However, it will be subjected to combine bending and tension when a middle column is removed. Previous works [12, 39] indicated that the current acceptance criteria of rotation capacity for RBS connection are probably too conservative. Plastic hinge formed in RBS connection would help to enhance its rotation capacity and enable full development of tying capacity. Thus, it was necessary to develop a calculation model for quantify the tying capacity of RBS connections.

According to Chapter H of ANSI/AISC 360-10 [37], the required axial strength P_r were corrected owing to the presence of the bending moment. The tying capacity of RBS connection can be determined by Eq. 6:

$$\begin{cases} P_r \leq P_c\left[1.0-\dfrac{8}{9}\left(\dfrac{M_{rx}}{M_{cx}}+\dfrac{M_{rx}}{M_{cx}}\right)\right], & when\ P_r \geq 0.2P_c \\ P_r \leq 2P_c\left[1.0-\left(\dfrac{M_{rx}}{M_{cx}}+\dfrac{M_{rx}}{M_{cx}}\right)\right], & when\ P_r < 0.2P_c \end{cases} \tag{6}$$

where P_c is the available axial strength, M_r and M_c are the required and available flexural strength, and x and y are the subscript to represent strong axis and weak axis, respectively.

As the tensile force dominated the behavior and failure mode of RBS at large deformation stage, Yang and Tan [16] proposed the tying resistance of the connections equal to the contribution of CA.

Thus, the tying resistance P_r' of RBS connection can be described as followed:

$$P_r' = P_r \sin\theta_c \tag{7}$$

where θ_c is the rotation capacity of RBS connections.

The probable maximum moment at the center of reduced beam section specified in FEMA 350 [32] is evaluated based on the yield capacity. As mentioned above, the capacity of RBS exceeded the ultimate capacity of RBS under combined axial and flexural loads. Similar observation was concluded by Sadek et al. [40]. This implies that the acceptance criteria give a low-bound estimation for RBS connection.

5. Numerical analysis

5.1. Numerical model

To further investigate the behavior of steel sub-frames with RBS against progressive collapse, FE models using explicit software LS-DYNA [41] were employed due to its numerical stability and variety of constitutive models [42-50]. Many other software has been used in progressive collapse analysis [51], however, it is found that LS-DYNA is one of the most powerful software. Therefore, it is used here. The FE models were validated by comparing with experimental results. As shown in Fig.

18a, boundary conditions applied on the FE models replicates that from the experimental tests. Due to the complication in simulation of horizontal constraints (inevitable gaps exists in rollers), springs was used to simulate the horizontal constraints at the overhanging beams, as shown in Fig. 18b. The stiffness of the springs was determined based on the measured horizontal reaction force of the roller and lateral displacements, as shown in Table 3. A vertical displacement was applied at the middle column. In order to avoid dynamic vibration due to step force, smooth step amplitude displacement control was used. Further, the ratio of the kinetic energy and external work was maintained less than 1 % [39].

Fig. 18b shows the FE model of the specimen. The beam/columns were simulated by 8-node solid elements with a reduced integration, but the springs used discrete elements. As numerical results are sensitive to the material properties, adopting appropriate constitutive model is crucial. Within the material library of LS-DYNA, an isotropic elastic-plastic material model *Mat_Piecewise_Linear_Plasticity (MAT_024) was used for steel. The measurements showed that the deviations from the nominal geometries of the two specimens were very small. The FE models were created using the nominal values. The material properties were defined based on measured material property (see Table 1). Pin supports were simulated by using the keyword *CONSTRAINED_JOINT_REVOLUTE (see Fig. 18b).

Fig .19 shows the mesh of the joint zone with different sizes. For Mesh 1, 10 mm was meshed in the potential plastic hinge zone while remaining parts were meshed with size of 30 mm. For Mesh 2 and 3, the remaining parts were meshed with size of 20 mm and 10 mm, respectively. As shown in Fig. 20a, there was no big difference for Mesh 1, 2, and 3 in terms of initial stiffness, peak load, and deformation capacity. Therefore, Mesh 1 was selected in this numerical study due to computational cost consideration.

5.2. Verification of numerical model

Figs. 20-21 show the comparison of the experimental and numerical results. In generally, the numerical models agree well with the experimental results in terms of vertical load resistance, horizontal reaction force, and axial force in beams. Figs. 22 and 23 show the simulated failure mode of GBS and RBS, respectively. Comparing with test results, the fracture of the connection and plastic deformation of the connections were well simulated. Thus, it was reliable to adopt the validated FE models for further parametric study.

6. Parametric study

Based on the validated models, the effects of span/depth ratio and other section reduction method on behavior of steel frames to resist progressive collapse were quantified.

6.1. Span/depth ratio

Fig. 24 illustrates the influence of different span/depth ratio k on load resistance of RBS. where $k = L/d_{beam}$, L represents the beam span and d_{beam} represents the height of beam. Moreover, d_{beam} keeps constant and beam span increases with increase of the span/depth ratio. As shown in the figure, when k decreased from 15 to 10, the PL increased by 12.1 % and the ultimate deformation capacity decreased by 31.0 %. However, when k increased from 15 to 22.5 and 30, the deformation capacity increased by 56.3 % and 102.3 %, respectively. However, the PL decreased by 3.3 % and 0.8 %, respectively. The deformation capacity of the specimen decreases with decrease of the span/depth ratio. However, it will not affect the PL significantly as PL was mainly controlled by catenary action. If the MCD was replaced by rotation, which was defined as the ratio of MCD to beam span, the span/depth ratio will affect the initial stiffness of the steel frame significantly. However, it will not affect the rotation capacity significantly, as shown in Fig. 24b.

6.2. Different section reduction methods

To investigate the collapse behavior of the welded connection with reduced beam section (i.e. reduced beam section) further, four reduction types are investigated (refer to Fig. 25). Morshedi et al. [52] provided a reference for the design of the double reduced beam section (DRBS) (refer to Fig. 25a). Opening in bean flange (OBW) (refer to Fig. 25b) is proposed by Chung et al. [53] as an effective method to improve the behavior of steel frame to resist progressive collapse. Meng [54] suggested an innovative method to punch an opening in bean flange (OBF) (refer to Figs. 25c and

25d), where OBF-2 and OBF-3 represent two and three holes in beam flange, respectively. However, the total opening area of OBF-2 and OBF-3 was identical.

6.2.1. Double reduced beam section

Fig. 26a compares the load resistance of RBS and DRBS. As can be seen from the figure, the curves almost coincide before the MCD of 36 mm (θ = 0.012 rad) in elastic stage. Similar to RBS, with increasing the vertical displacement, plastic hinges were formed at the position of reduced sections in DRBS. Actually, before fracture occurred in the beam of RBS, these two curves are similar. The PL of RBS and DRBS were 394.8 kN and 544.2 kN, respectively. The ultimate deformation capacity of RBS and DRBS were 435 mm (θ = 0.145 rad) and 529 mm (θ = 0.176 rad), respectively. Thus, DRBS could increase the PL and deformation capacity by 37.9 % and 21.5 %, respectively. The failure mode of DRBS is shown in Fig. 27.

6.2.2. Perforated beam section

OBW, OBF-2 and OBF-3 are perforated openings with same total opening area at the web or flanges base on the validated FE model of GBS. Fig. 26b compares the load resistance of GBS, OBW, OBF-2, and OBF-3. As can be seen from the figure, OBW achieved the highest PL and deformation capacity in these perforated beam section specimens. When MCD reached 30 mm (θ = 0.010 rad), plastic hinges concentrated in the perforated zone of the web and propagates rapidly. At MCD of 415 mm (θ = 0.138 rad) corresponding load resistance of 225.0 kN, BEMC-1 fractured at the bottom flange. At MCD of 500 mm (θ = 0.167 rad) and 550 mm (θ = 0.183 rad), bottom flanges in BEMC-1 and BEMC-2 completely fractured one by one. However, the load resistance did not decrease until the fracture propagated into the top flange and completely detached at MCD of 600 mm (θ = 0.200 rad). The failure mode of OBW is shown in Fig. 28. Completely fracture occurred in the center of opening of the beam web. Compared with GBS, the PL and deformation capacity of OBW was increased by 20.9 % and 76.5 %, respectively.

As shown in Fig. 26b, compared with GBS, the deformation capacity of OBF-2 and OBF-3 were increased by 44.8 % and 62.4 % respectively. However, the PL of OBF-2 and OBF-3 were only about 58.4 % and 79.6 % of that of GBS. Therefore, punching opening in the flange of the beam section will decrease the load resistance but increase the deformation capacity. OBF-3 performed much better than that of OBF-2 mainly due to larger opening size in OBF-2 although total opening area was same in these two models. The failure modes of OBW-2 and OBW-3 are shown in Figs. 29 and 30. The fracture of OBW-2 and OBW-3 first occurred in the perforated beam section of the flange.

7. Conclusions

The experimental investigations under a middle column removal scenario were carried out to study the behavior of steel substructures with welded connection with seismic configurations. Based on experimental results, detailed FE models were established to conduct parametric study using finite element software LS-DYNA. The following conclusions are drawn:

1. The experimental results indicated that the performance of welded connection with RBS was superior to the welded connection with GBS. The resistance and deformation capacity of RBS was 106.1 % and 24.1 % higher than that of GBS.
2. At the initial stage of column removal, the beams in different stories deform together. Thus, the beams in the first story suffered tension while the beams in the second story experienced compression. Looking at the load resistance, in relatively small deformation stage, the load resistance from the beams in the first story is higher than that of the beams in the second story. However, in large deformation stage, the load resistance of these two stories is similar for RBS. For GBS, the load resistance of the beams in the first story is much less than that from second story in large deformation stage may be due to undesired pre-mature fracture at the welding connection of the first story.
3. Experimental results indicated that flexural action and catenary action worked together to resist progressive collapse of the frame in large deformation stage. It was confirmed that measured rotation capacity of steel frames with welded connections, especially with reduced beam section, is much larger than the value predicted based on design code FEMA 350 [32].

4. Analytical results indicated that the measured bending moment capacity of critical section could exceed the yield bending moment capacity due to bending moment-tension composite action.
5. Numerical and parametric studies indicated that the deformation capacity of steel frames increase as the span-depth ratio increase. However, span-depth ratio has little effects on ultimate rotation capacity and ultimate load. Double reduced beam section could further upgrade the load resisting capacity and deformation capacity of the steel frames. Punched openings in the beam flange will decrease the initial stiffness and load resistance but increase the deformation capacity significantly.
6. Catenary action contributes to arrest progressive collapse of steel structures at large deformation stage, therefore, sufficient deformation capacity of the connection should be designed. This implies that engineers could adopt effective section reduction methods to motivate catenary action of the steel frames adequately, but it should be taken in moderation due to the decrease of its load resisting capacity.

Acknowledgements

This research was supported by a research grant provided by the Natural Science Foundation of China (Nos.51778153, 51568004), and Guangxi university postgraduate education innovation program (No. YCBZ2019024). Any opinions, findings and conclusions expressed in this paper do not necessarily reflect the view of Natural Science Foundation of China.

Future work

As the next steps in this research program, we intend to perform more experimental study taking into consideration infilled wall with the steel moment frames under the middle column removal scenario.

References

[1] C. Málaga-Chuquitaype, A.Y. Elghazouli, R. Enache, Contribution of secondary frames to the mitigation of collapse in steel buildings subjected to extreme loads, Struct. Infrastruct. Eng. 12(1) (2016) 45-60.

[2] E. Stoddart, M. Byfield, B. Davison, A. Tyas, Strain rate dependent component based connection modelling for use in non-linear dynamic progressive collapse analysis, Eng. Struct. 55 (2013) 35-43.

[3] O.A. Mohamed, Calculation of load increase factors for assessment of progressive collapse potential in framed steel structures, Case Stud. Struct. Eng. 3 (2015) 11-18.

[4] J.J. Mashhadi, H. Saffari, Dynamic increase factor based on residual strength to assess progressive collapse, Steel Comp. Struct. 25(5) (2017) 617-624.

[5] A. McKay, K. Marchand, M. Diaz, Alternate path method in progressive collapse analysis: variation of dynamic and nonlinear load increase factors. Practice periodical on structural design and construction, Pract. Period. Struct. Des. Constr. 17(4) (2012) 152-160.

[6] M. Liu, A new dynamic increase factor for nonlinear static alternate path analysis of building frames against progressive collapse, Eng. Struct. 48 (2013) 666-673.

[7] M. Ferraioli, Dynamic increase factor for pushdown analysis of seismically designed steel moment-resisting frames, Int. J. Steel Struct. 16(3) (2016) 857-875.

[8] M. Ferraioli, A. Lavino, A. Mandara, Dynamic increase factor for nonlinear static alternate path analysis of steel moment-resisting frames against progressive collapse, ce/papers (2017).

[9] M. Ferraioli, A modal pushdown procedure for progressive collapse analysis of steel frame structures, J. Constr. Steel Res. 156 (2019) 227-241.

[10] T. Kim, J. Kim, J. Park, Investigation of progressive collapse-resisting capability of steel moment frames using push-down analysis, J. Perform. Constr. Facil. 23(5) (2009) 327-335.

[11] M. Ferraioli, Evaluation of dynamic increase factor in progressive collapse analysis of steel frame structures considering catenary action, Steel Comp. Struct. 30(3) (2019) 253-269.

[12] H.S. Lew, J.A. Main, S.D. Robert, et al., Performance of steel moment connections under a column removal scenario. I: Experiments, J. Struct. Eng. 139 (1) (2013) 98-107.

[13] W.H. Zhong, B. Meng, J.P. Hao, Performance of different stiffness connections against progressive collapse, J. Constr. Steel Res. 135 (2017) 162-175.

[14] B. Meng, W.H. Zhong, J.P. Hao, Anti-collapse performances of steel beam-to-column assemblies with different span ratios, J. Constr. Steel Res. 140 (2018) 125-138.
[15] M. Xu, S. Gao, L.H. Guo, et al., Study on collapse mechanism of steel frame with CFST-columns under column-removal scenario, J. Constr. Steel Res. 141 (2018) 275-286.
[16] B. Yang, K.H. Tan, Experimental tests of different types of bolted steel beam-column joints under a central-column-removal scenario, Eng. Struct. 54 (2013) 112-130.
[17] L. Li, W. Wang, Y.Y. Chen, Y. Lu, Experimental investigation of beam-to-tubular column moment connections under column removal scenario, J. Constr. Steel Res. 88 (2013) 244-255.
[18] L. Li, W. Wang, Y.Y. Chen, Y. Lu, Effect of beam web bolt arrangement on catenary behaviour of moment connections, J. Constr. Steel Res. 104 (2015) 22-36.
[19] M. Xu, S. Gao, S.M. Zhang, H.H. Li, Experimental study on bolted CFST-column joints with different configurations in accommodating column-loss, J. Constr. Steel Res. 151 (2018) 122-131.
[20] S. Gao, M. Xu, F. Fu, L.H. Guo, Performance of bolted steel-beam to CFST-column joints using stiffened angles in column-removal scenario, J. Constr. Steel Res. 159 (2019) 459-475.
[21] L.H. Guo, S. Gao, F. Fu, Y.Y. Wang, Experimental study and numerical analysis of progressive collapse resistance of composite frames, J. Constr. Steel Res. 89 (2013) 236-251.
[22] B. Yang, K.H. Tan, G. Xiong, S.D. Nie, Experimental study about composite frames under an internal column-removal scenario, J. Constr. Steel Res. 121 (2016) 341-351.
[23] S.B. Kang, K.H. Tan, H.Y. Liu, et al., Effect of boundary conditions on the behaviour of composite frames against progressive collapse, J. Constr. Steel Res. 138 (2017) 150-167.
[24] S. Gao, L.H. Guo, F. Fu, S.M. Zhang, Capacity of semi-rigid composite joints in accommodating column loss, J. Constr. Steel Res. 139 (2017) 288-301.
[25] R. Zandonini, N. Baldassino, F. Freddi, G. Roverso, Steel-concrete frames under the column loss scenario: An experimental study, J. Constr. Steel Res. 162 (2019) UNSP 105527.
[26] G.C. Zhou, J. Shi, P.C. Li, H.H. Li, Characteristics of structural state of stress for steel frame in progressive collapse, J. Constr. Steel Res. 160 (2019) 444-456.

[27] J.J. Wang, W. Wang, Y.H. Bao, D. Lehman, Full-scale test of a steel moment-resisting frame with composite floor under a penultimate edge column removal scenario, J. Constr. Steel Res. 162 (2019) UNSP 105717.

[28] J.J. Wang, W. Wang, D. Lehman, C. Roeder, Effects of different steel-concrete composite slabs on rigid steel beam-column connection under a column removal scenario, J. Constr. Steel Res. 153 (2019) 55-70.

[29] G.Q. Li, L.L. Li, B.H. Jiang, Y. Lu, Experimental study on progressive collapse resistance of steel frames under a sudden column removal scenario, J. Constr. Steel Res. 147 (2018) 1-15.

[30] L.L. Li, G.Q. Li, B.H. Jiang, Y. Lu, Analysis of robustness of steel frames against progressive collapse, J. Constr. Steel Res. 143 (2018) 264-278.

[31] American Institute of Steel Construction, Seismic Provisions for Structural Steel Buildings. ANSI/AISC 341-10, Chicago, USA 2010.

[32] Federal Emergency Management Agency, Recommended Seismic Design Criteria for New Steel Moment-Frame Buildings. FEMA 350, Washington (DC), USA 2000.

[33] H.H. Li, X.H. Cai, L. Zhang, et al., Progressive collapse of steel moment-resisting frame subjected to loss of interior column: Experimental tests, Eng. Struct. 150 (2017) 203-220.

[34] B. Yang, K.H. Tan, Numerical analyses of steel beam-column joints subjected to catenary action, J. Constr. Steel Res. 70 (2012) 1-11.

[35] B. Yang, K.H. Tan, G. Xiong, Behaviour of composite beam–column joints under a middle-column-removal scenario: Component-based modelling, J. Constr. Steel Res. 104 (2015) 137-154.

[36] F. Fu, Progressive collapse analysis of high-rise building with 3-D finite element modeling method, J. Constr. Steel Res. 65 (6) (2009) 1269–1278.

[37] American Institute of Steel Construction, Specification for Structural Steel Buildings. ANSI/AISC 360-10, Chicago, USA 2010.

[38] American Institute of Steel Construction, Prequalified Connections for Special and Intermediate Steel Moment Frames for Seismic Applications. ANSI/AISC 358-10, Chicago, USA 2010.

[39] F. Dinu, I. Marginean, D. Dubina, Experimental testing and numerical modelling of steel moment-frame connections under column loss, Eng. Struct. 151 (2017) 861-878.

[40] F. Sadek, J.A. Main, H.S. Lew, S. El-Tawil, Performance of steel moment connections under a column removal scenario. II: Analysis, J. Struct. Eng. 139 (1) (2013) 108-119.

[41] J. Hallquist, LS-DYNA keyword user's manual, Version 971, Livermore Software Technology Corp., Livermore, CA, 2007.

[42] M. Yu, X.X. Zha, J.Q. Ye, The influence of joints and composite floor slabs on effective tying of steel structures in preventing progressive collapse, J. Constr. Steel Res. 66 (2010) 442-451.

[43] C.G. Tay, C.G. Koh, J.Y.R. Liew, Efficient progressive collapse analysis for robustness evaluation of buildings experiencing column removal, J. Constr. Steel Res. 122 (2016) 395-408.

[44] H. Wang, B. Yang, X.H. Zhou, S.B. Kang, Numerical analyses on steel beams with fin-plate connections subjected to impact loads, J. Constr. Steel Res. 124 (2016) 101-112.

[45] Y. Ding, X.R. Song, H.T. Zhu, S.B. Kang, Probabilistic progressive collapse analysis of steel-concrete composite floor systems, J. Constr. Steel Res. 129 (2017) 129-140.

[46] B. Yang, H. Wang, Y. Yang, et al., Numerical study of rigid steel beam-column joints under impact loading, J. Constr. Steel Res. 147 (2018) 62-73.

[47] S.C. Lin, B. Yang, S.B. Kang, S.Q. Xu, A new method for progressive collapse analysis of steel frames, J. Constr. Steel Res. 153 (2019) 71-84.

[48] X. F. Deng, S. L. Liang, F. Fu, K. Qian, Effects of high-strength concrete on progressive collapse resistance of reinforced concrete frame. Journal of Structural Engineering. 146(6) (2020)04020078.

[49] K. Qian, S. L. Liang, X. Y. Xiong, F. Fu, Q. Fang, Quasi-static and dynamic behavior of precast concrete frames with high performance dry connections subjected to loss of a penultimate column scenario. Engineering Structures. 205(2020) 110115.

[50] Y. H. Weng, K. Qian, F. Fu, Q. Fang. Numerical investigation on load redistribution capacity of flat slab substructures to resist progressive collapse, Journal of Building Engineering. 29(2020), 101109.

[51] Fu, F.(2016) Structural Analysis and Design to Prevent Disproportionate Collapse. CRC Press. ISBN 978-1-4987-8820-5

[52] M.A. Morshedi, K.M. Dolatshahi, S. Maleki. Double reduced beam section connection, J. Constr. Steel Res. 138 (2017) 283-297.

[53] K.F. Chung, T.C.H. Liu, A.C.H. Ko, Investigation on Vierendeel mechanism in steel beams with circular web openings, J. Constr. Steel Res. 57 (5) (2001) 467-490.

[54] Q.X. Meng, Research on seismic behavior of beam-to-column joint with beam flange openings, Hebei University of Engineering 2017 (in Chinese).

Table 1-Material properties from coupon test of the connection

Element	t (mm)	f_y (MPa)	μ_y	f_u (MPa)	f_f (MPa)	A_{gt} (%)
Beam flange	8.0	310	0.0019	420	315	12.0
Beam web	5.5	320	0.0021	430	340	13.5
Column flange	10.0	300	0.0019	410	300	14.0
Column web	7.0	295	0.0023	375	265	13.0

Note : t = plate thickness; f_y = yield strength; μ_y = yield stain; f_u = tensile strength; f_f = fracture strength (engineering stress); A_{gt} = total elongation at maximum stress.

Table 2-Test results

Specimen identifier	u_{YL} (mm)	θ_{YL} (rad)	F_{YL} (kN)	K_{YL} ($\times 10^3$ kN/m)	u_{PL} (mm)	θ_{PL} (rad)	F_{PL} (kN)	M_{max} (kN·m)	N_{max} (kN)
GBS	45	0.015	147.8	3.3	200	0.067	197.5	463.1	661.9
RBS	37	0.012	106.8	2.9	468	0.156	407.0	382.7	1712.4

Note: F_{YL} and F_{PL} = yield load and peak load capacity; u_{YL} and u_{PL} = displacements corresponding the yield load and peak load; K_{YL} = stiffness corresponding the yield load; θ_{YL} and θ_{PL}= chord rotation corresponding the yield and peak load; M_{max} and N_{max} = maximum bending moment and maximum axial force.

Table 3-Stiffness horizontal restraints

Element	Horizontal restraints	Stiffness ($\times 10^3$ N/mm)	Gap (mm)
GBS	1st story	46.4	0.5
	2nd story	51.0	4.1
RBS	1st story	39.2	0.7
	2nd story	31.0	0.9

List of Figures

Fig. 1 Location of the extracted frame in the prototype building (unit in mm): (a) plan view; (b) elevation view

Fig. 2 Dimensions of the specimen and locations of strain gauge and displacement transducers (unit in mm)

Fig. 3 Details of test specimens (unit in mm): (a) GBS; (b) RBS

Fig. 4 Test setup

Fig. 5 Comparison of the load-displacement curves

Fig. 6 Failure mode of GBS

Fig. 7 Failure mode of RBS

Fig. 8 Horizontal movement of the side column: (a) GBS; (b) RBS

Fig. 9 Overall deflection profile of the beams in the first story: (a) GBS; (b) RBS

Fig. 10 Horizontal reaction force-middle column displacement curves: (a) GBS; (b) RBS

Fig. 11 Internal forces at section B10 and B9

Fig. 12 Comparisons of vertical load resistance and horizontal reaction force from strain gauge and load cells (a) GBS; (b) RBS

Fig. 13 Variation of total bending moment and axial force of GBS and RBS

Fig. 14 De-composition of the load resistance from different actions: (a) GBS (b) RBS (Note: FA and CA represent flexural action and catenary action, respectively)

Fig. 15 De-composition of load resistance from 1st story and 2nd story: (a) GBS; (b) RBS

Fig. 16 Comparisons of the bending moment and axial force variation in 1st story and 2nd stories: (a) GBS; (b) RBS

Fig. 17 Bending moment-axial force interaction diagram

Fig. 18 Geometric model with boundary conditions: (a) overall view; (b) zone-in view

Fig. 19 Mesh configuration for different mesh strategy

Fig. 20 Comparison of experimental and numerical results of GBS: (a) vertical force; (b) horizontal reaction force; (c) axial force in beams

Fig. 21 Comparison of experimental and numerical results of RBS: (a) vertical force; (b) horizontal reaction force; (c) axial force in beams

Fig. 22 Comparison of the failure mode of GBS from test and numerical model

Fig. 23 Comparison of the failure mode of RBS from test and numerical model

Fig. 24 Investigation on effects of span-depth ratio (k): (a) vertical force vs. MCD; (b) vertical force vs. rotation

Fig. 25 Details of different types of reduced beam section (unit in mm): (a) DRBS; (b) OBW; (c) OBF-2; (d) OBF-3

Fig. 26 Comparison of the load-displacement response: (a) RBS and DRBS; (b) GBS, OBW, OBF-2, and OBF-3

Fig. 27 Failure mode of DRBS: (a) overall view; (b) zone-in view

Fig. 28 Failure mode of OBW: (a) overall view; (b) zone-in view

Fig. 29 Failure mode of OBF-2: (a) overall view; (b) zone-in view

Fig. 30 Failure mode of OBF-3: (a) overall view; (b) zone-in view

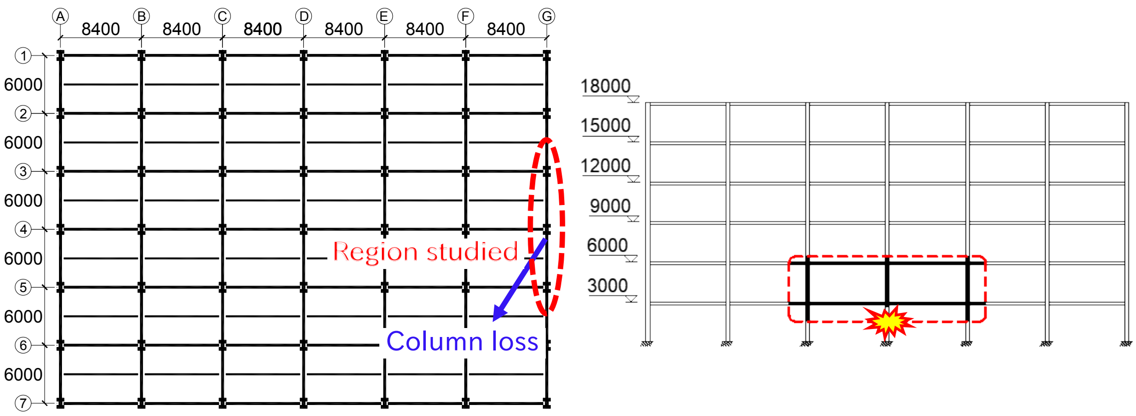

(a) (b)

Fig. 1 Location of the extracted frame in the prototype building (unit in mm): (a) plan view; (b) elevation view

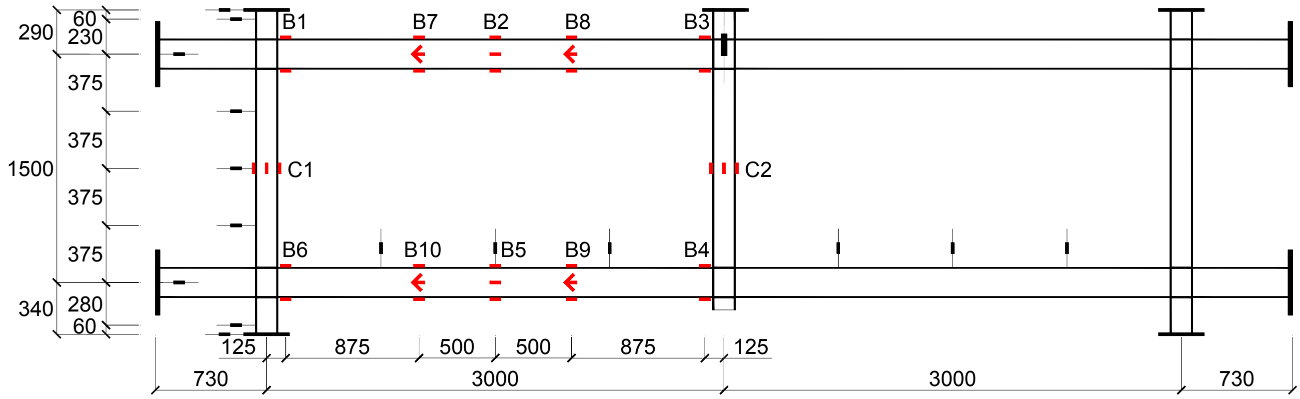

(a) Arrangements of strain gauges/rosettes and displacement transducers

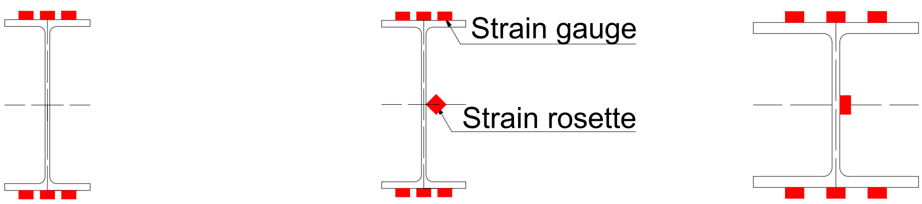

(b) Section B1 to B6 (c) Section B7 to B10 (d) Section C1 and C2

Fig. 2 Dimensions of the specimen and locations of strain gauge and displacement transducers (unit in mm)

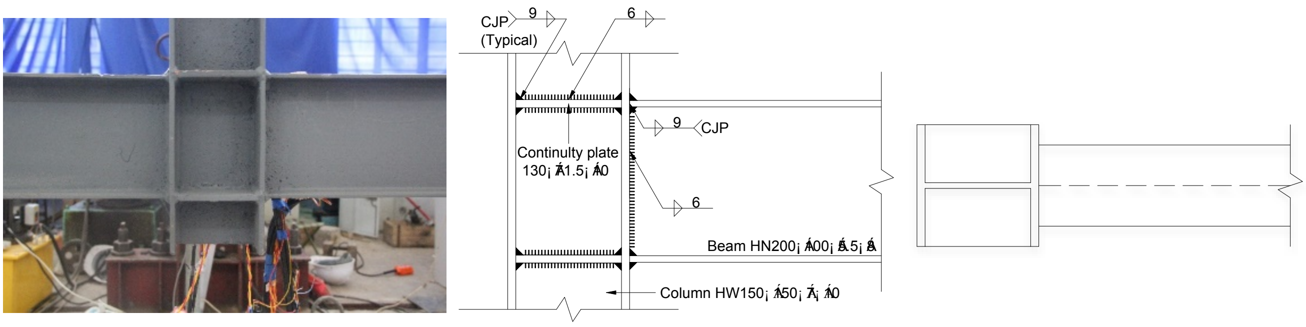

(a)

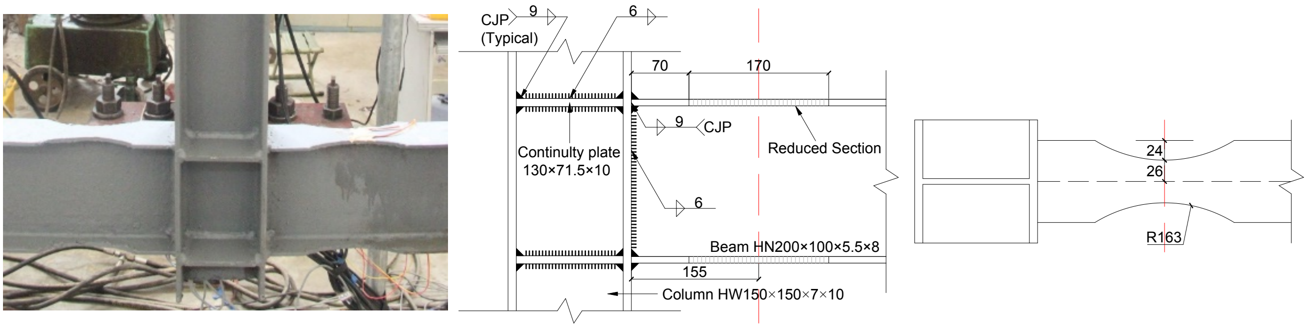

(b)

Fig. 3 Details of test specimens (unit in mm): (a) GBS; (b) RBS

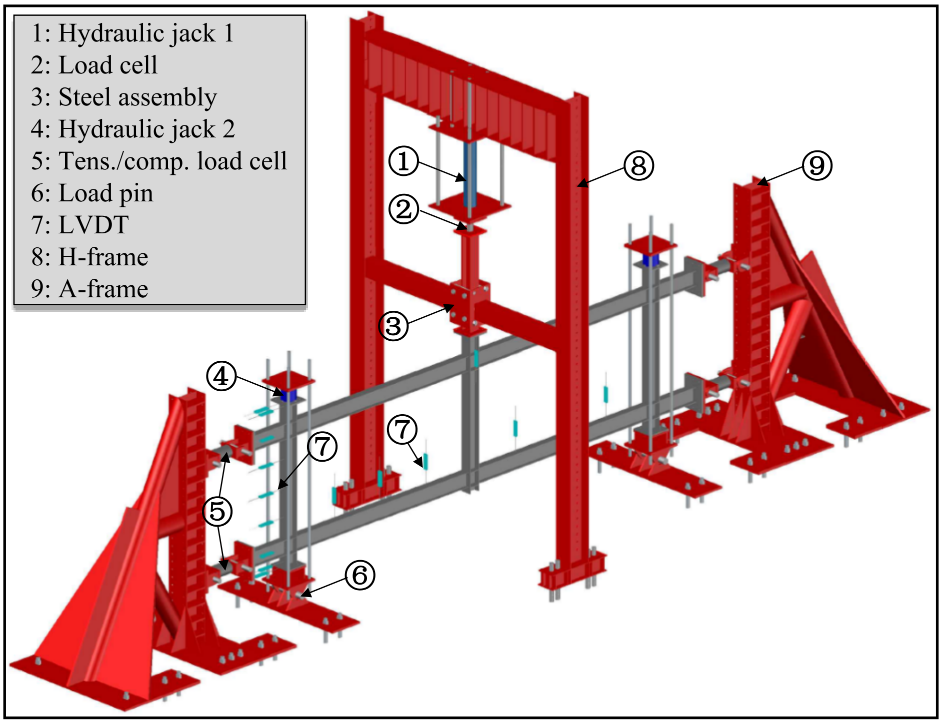

Fig. 4 Test setup

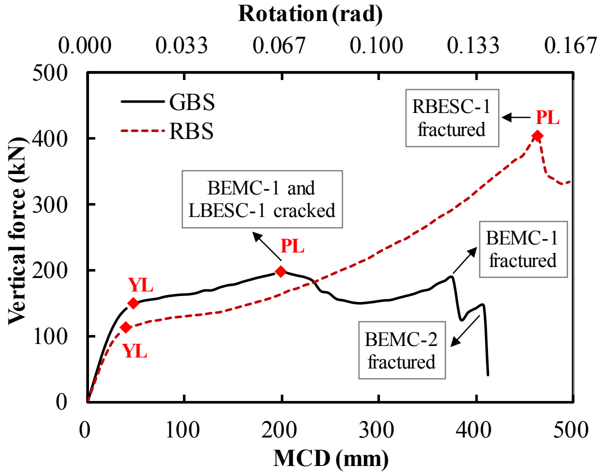

Fig. 5 Comparison of the load-displacement curves

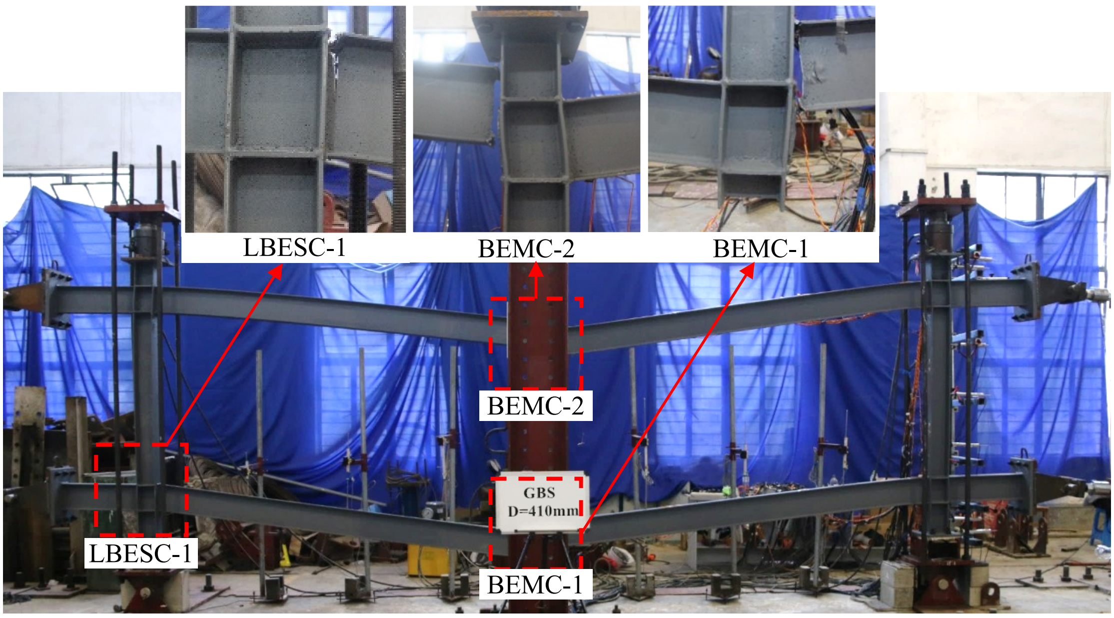

Fig. 6 Failure mode of GBS

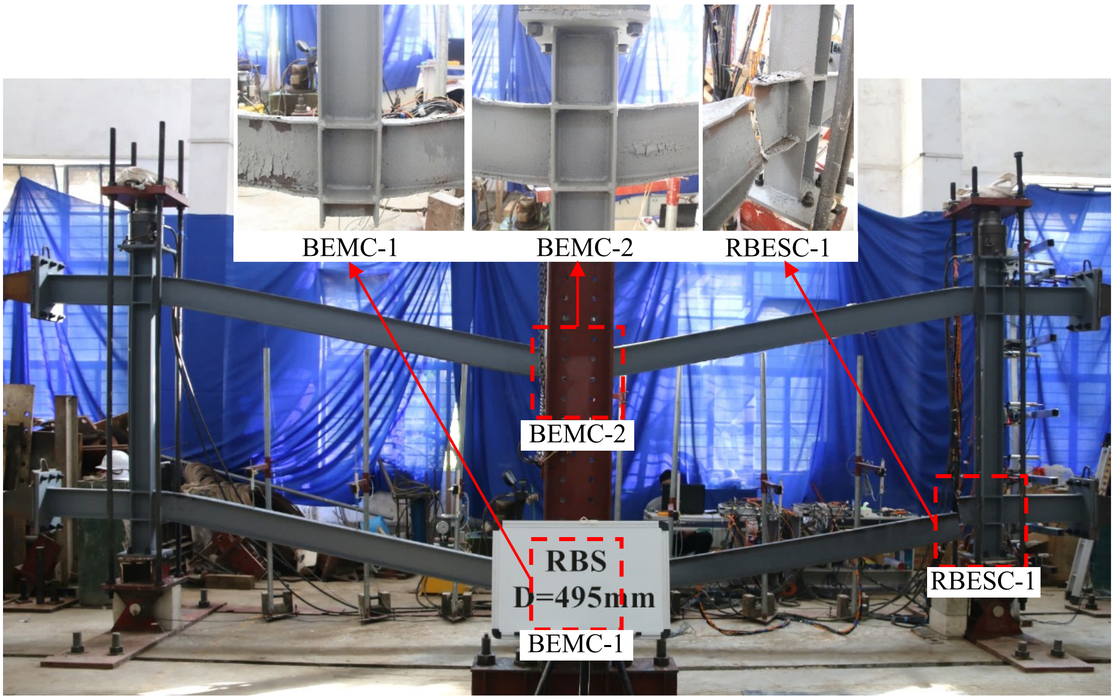

Fig. 7 Failure mode of RBS

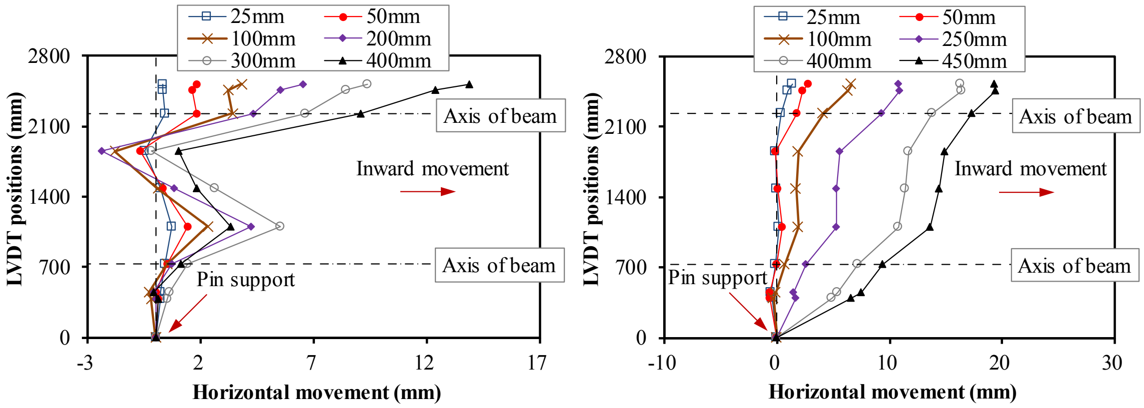

(a) (b)

Fig. 8 Horizontal movement of the side column: (a) GBS; (b) RBS

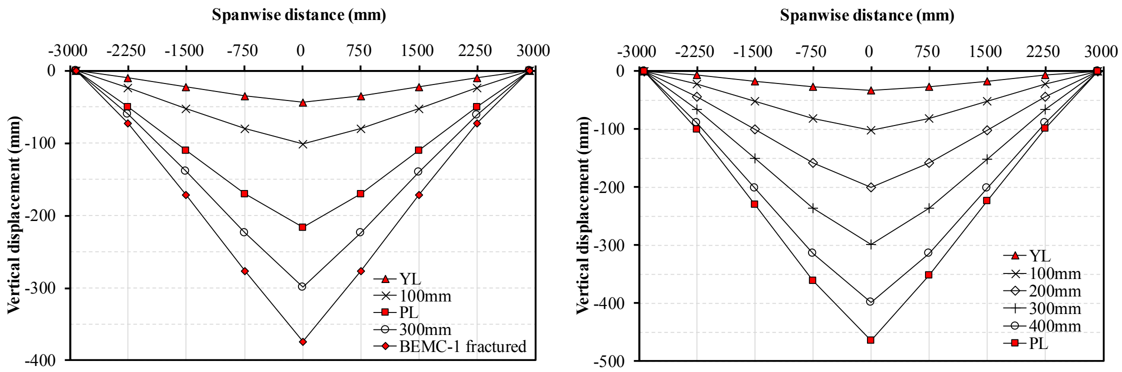

(a) (b)

Fig. 9 Overall deflection profile of the beams in the first story: (a) GBS; (b) RBS

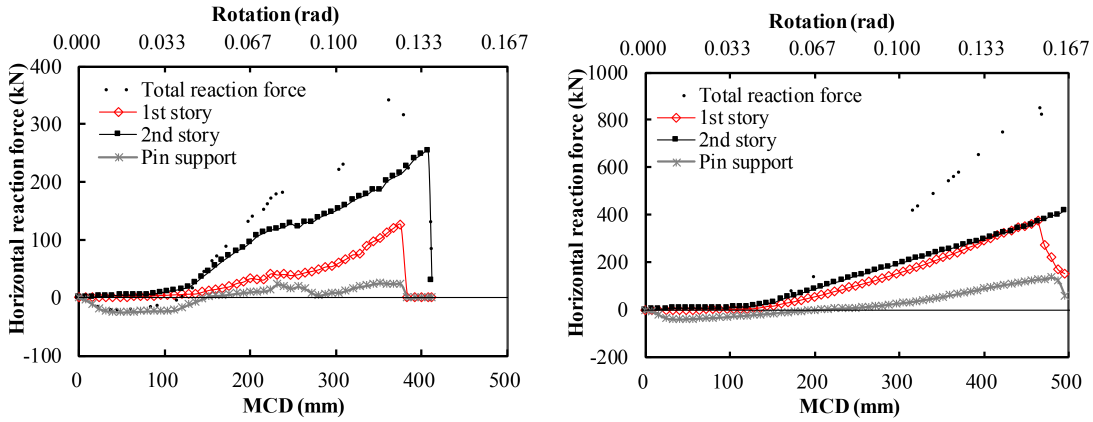

(a) (b)

Fig. 10 Horizontal reaction force-middle column displacement curves: (a) GBS; (b) RBS

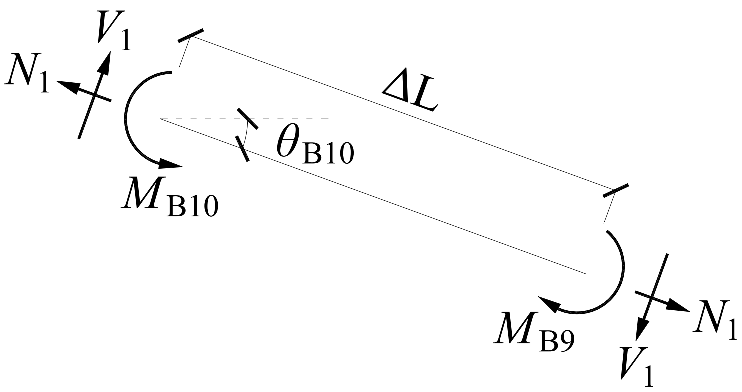

Fig. 11 Internal forces at section B10 and B9

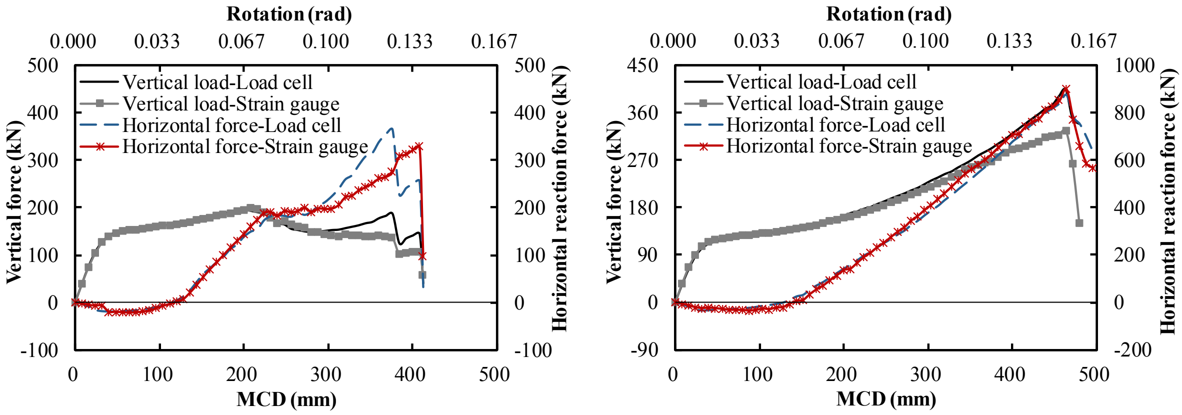

(a)

(b)

Fig. 12 Comparisons of vertical load resistance and horizontal reaction force from strain gauge and load cells: (a) GBS; (b) RBS

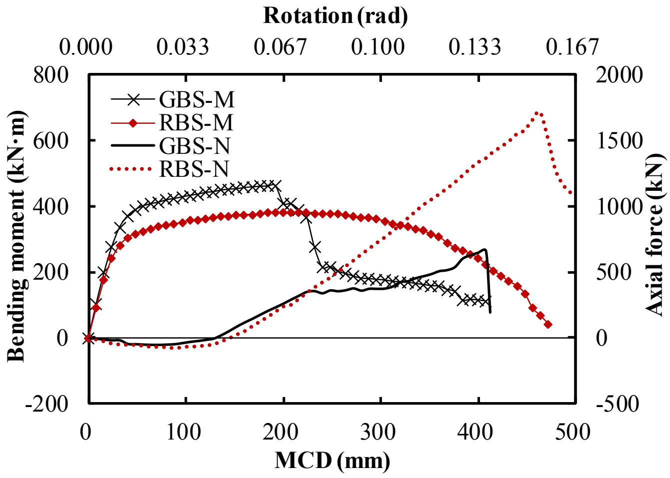

Fig. 13 Variation of total bending moment and axial force of GBS and RBS

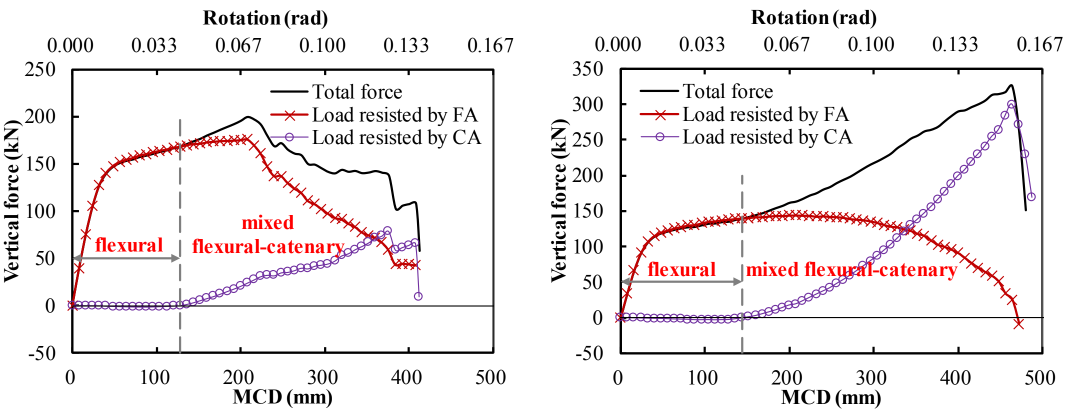

(a)

(b)

Fig. 14 De-composition of the load resistance from different actions: (a) GBS (b) RBS

(Note: FA and CA represent flexural action and catenary action, respectively)

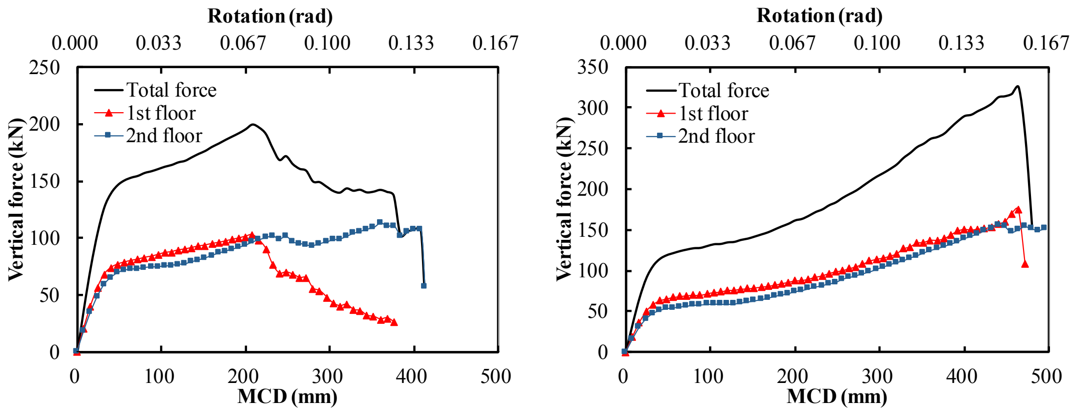

(a) (b)

Fig. 15 De-composition of load resistance from 1st story and 2nd story: (a) GBS; (b) RBS

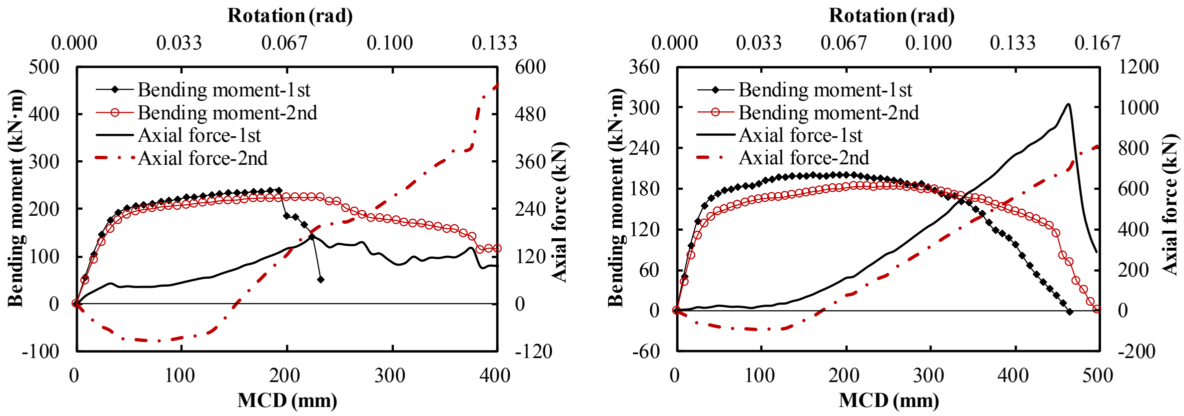

(a) (b)

Fig. 16 Comparisons of the bending moment and axial force variation in 1st story and 2nd stories: (a) GBS; (b) RBS

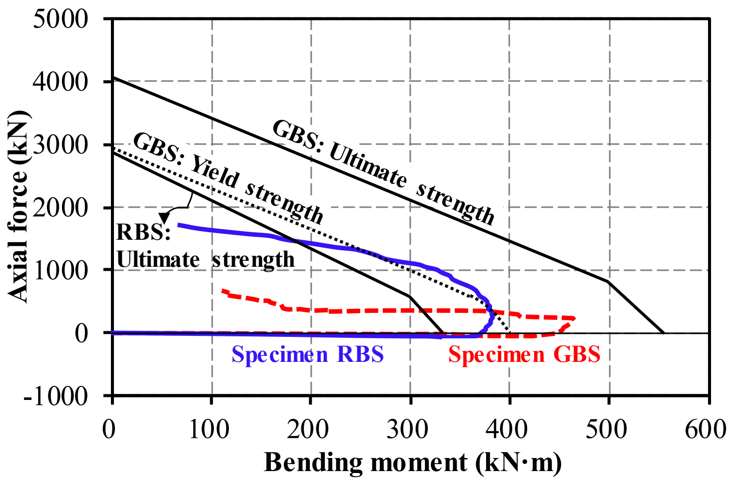

Fig. 17 Bending moment-axial force interaction diagram

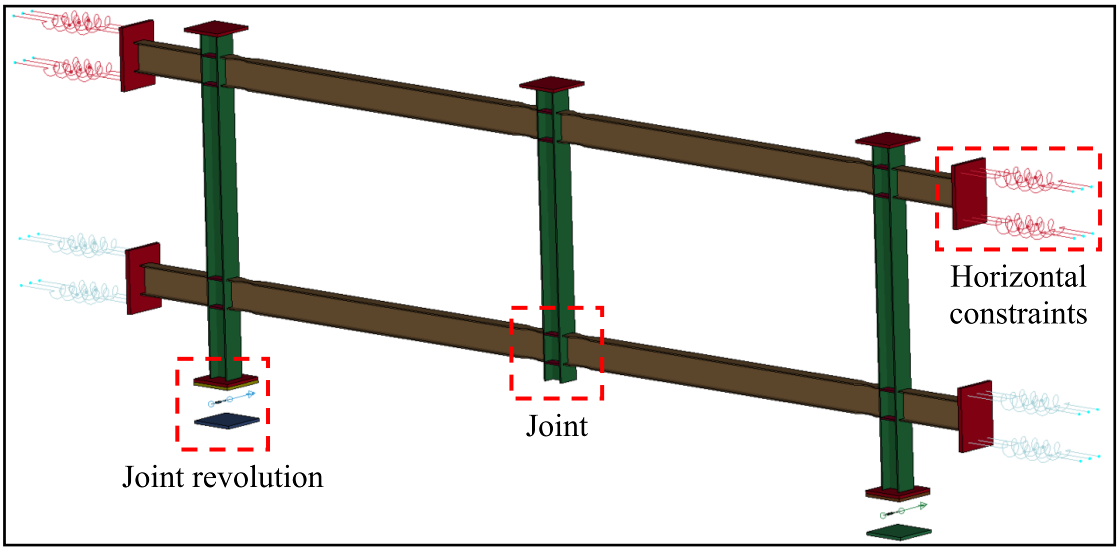

(a)

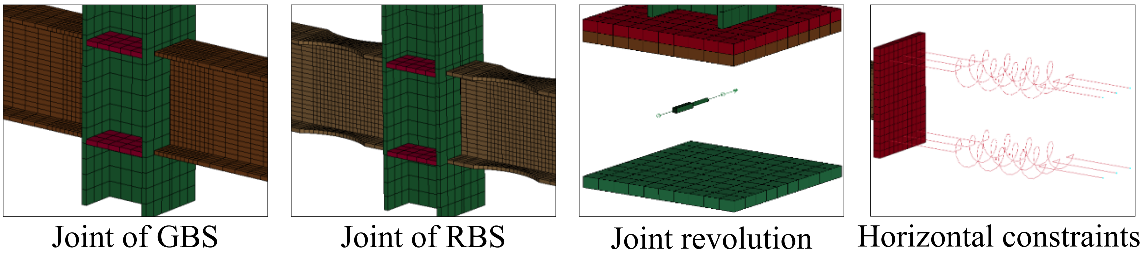

(b)

Fig. 18 Geometric model with boundary conditions: (a) overall view; (b) zone-in view

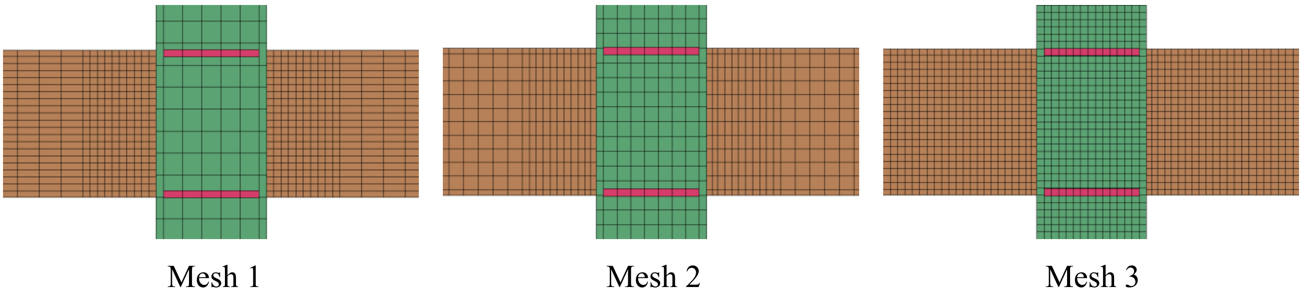

Fig. 19 Mesh configuration for different mesh strategy

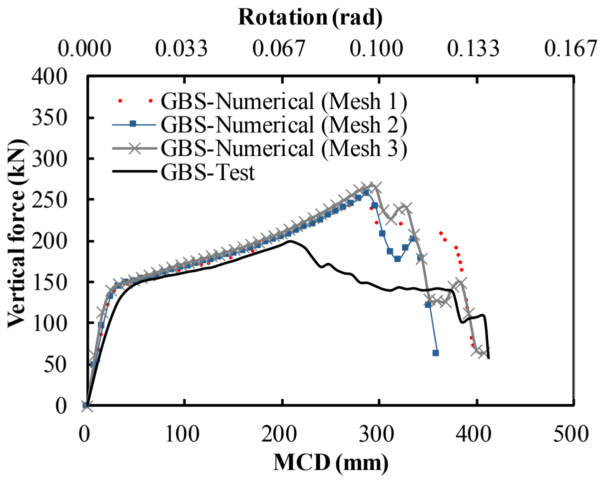

(a)

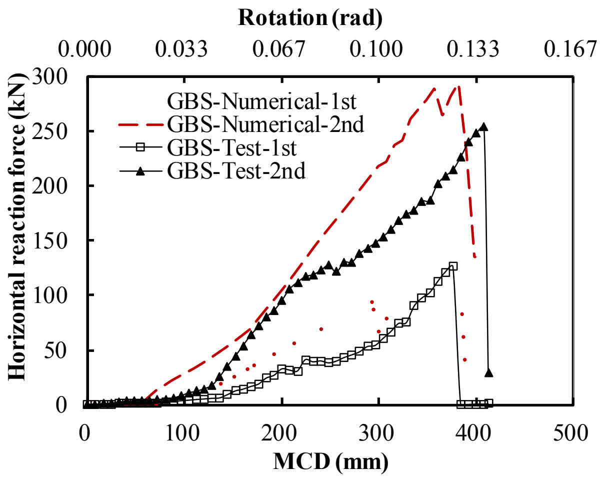

(b)

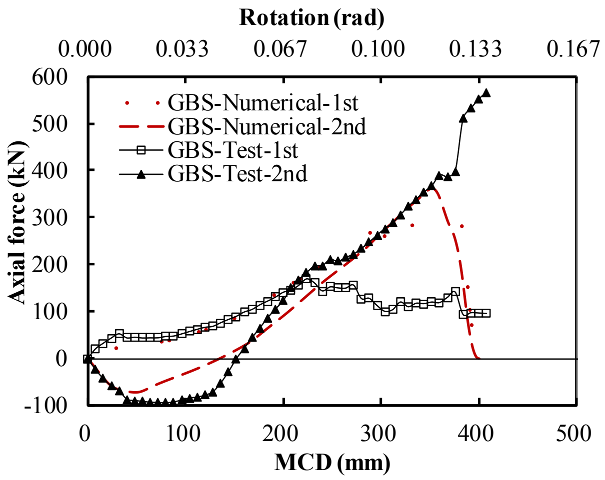

(c)

Fig. 20 Comparison of experimental and numerical results of GBS: (a) vertical force; (b) horizontal reaction force; (c) axial force in beams

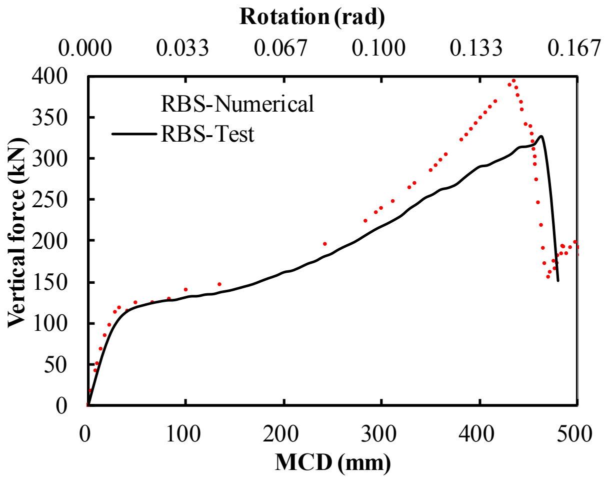

(a)

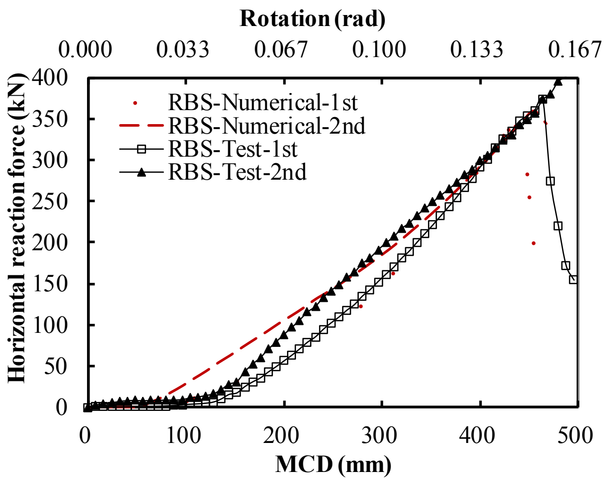

(b)

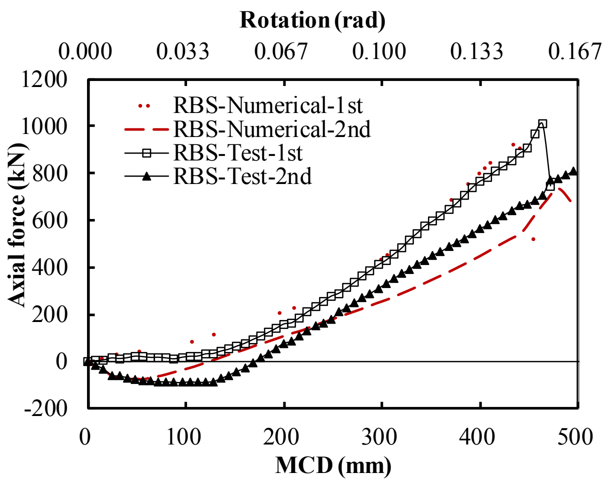

(c)

Fig. 21 Comparison of experimental and numerical results of RBS: (a) vertical force; (b) horizontal reaction force; (c) axial force in beams

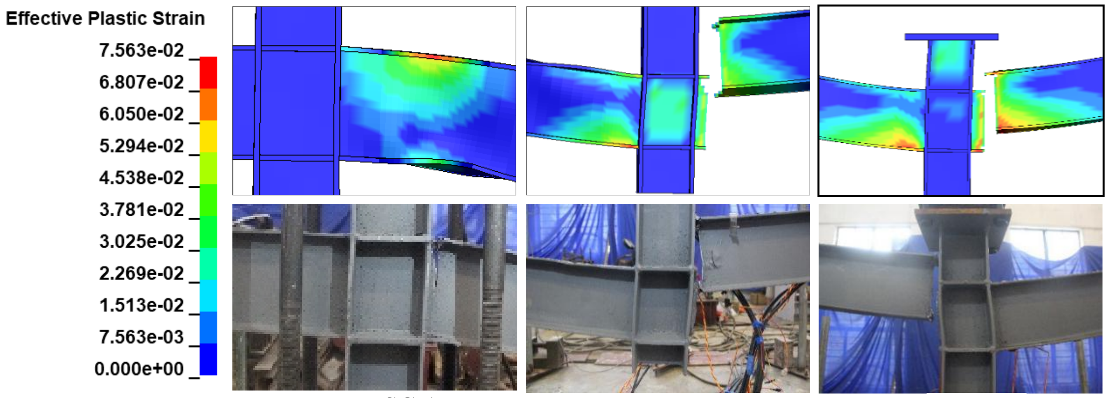

Fig. 22 Comparison of the failure mode of GBS from test and numerical model

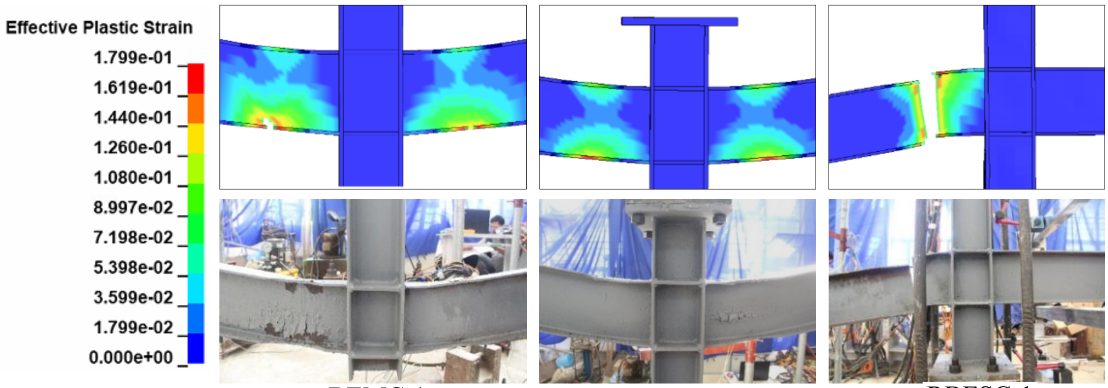

Fig. 23 Comparison of the failure mode of RBS from test and numerical model

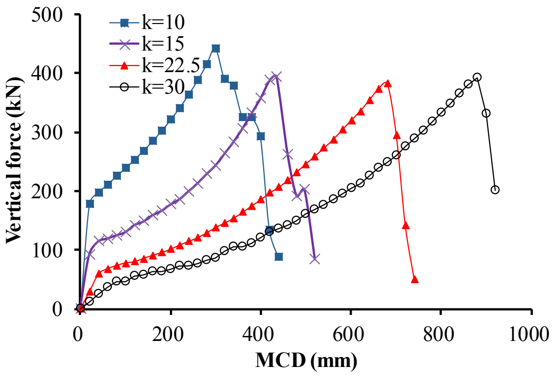

(a)

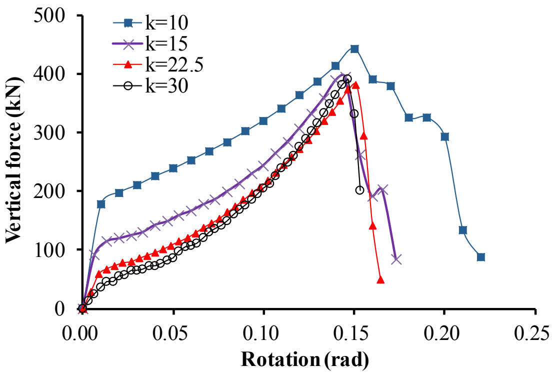

(b)

Fig. 24 Investigation on effects of span-depth ratio (k): (a) vertical force vs. MCD; (b) vertical force vs. Rotation

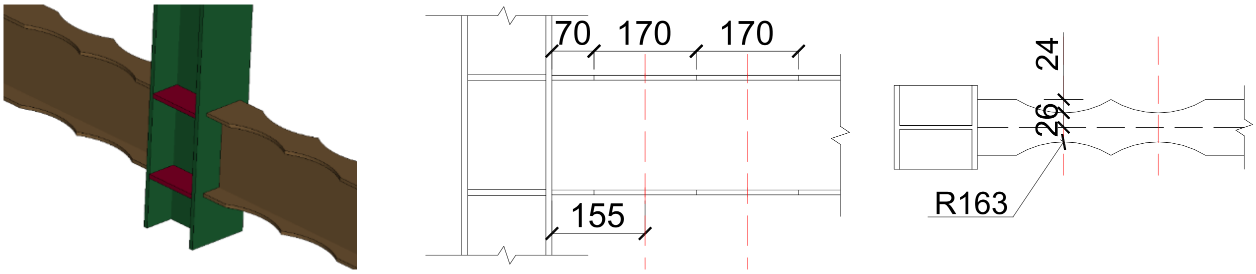

(a)

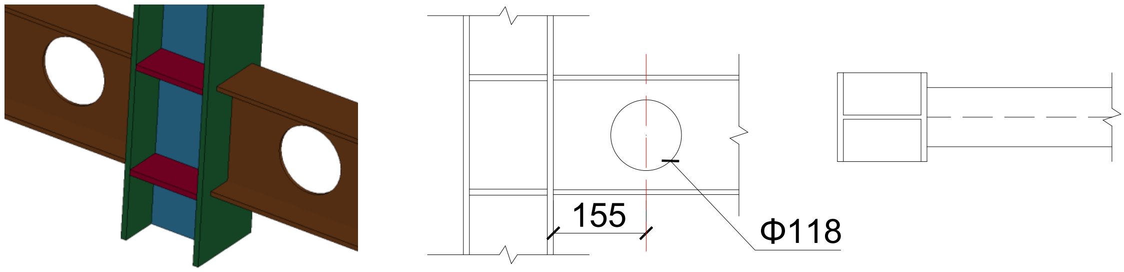

(b)

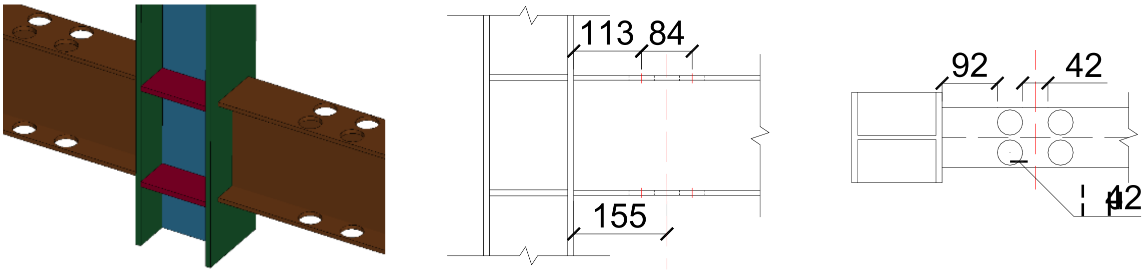

(c)

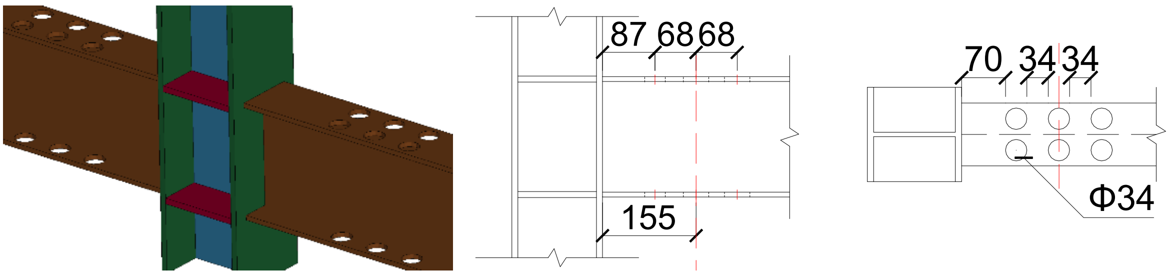

(d)

Fig. 25 Details of different types of reduced beam section (unit in mm): (a) DRBS; (b) OBW; (c) OBF-2; (d) OBF-3

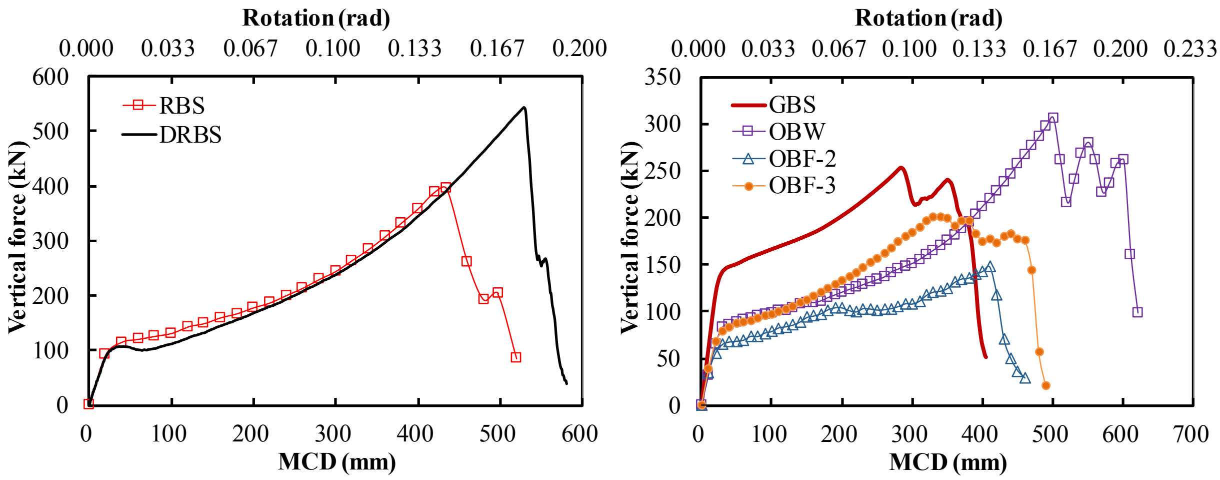

(a) (b)

Fig. 26 Comparison of the load-displacement response: (a) RBS and DRBS; (b) GBS, OBW, OBF-2, and OBF-3

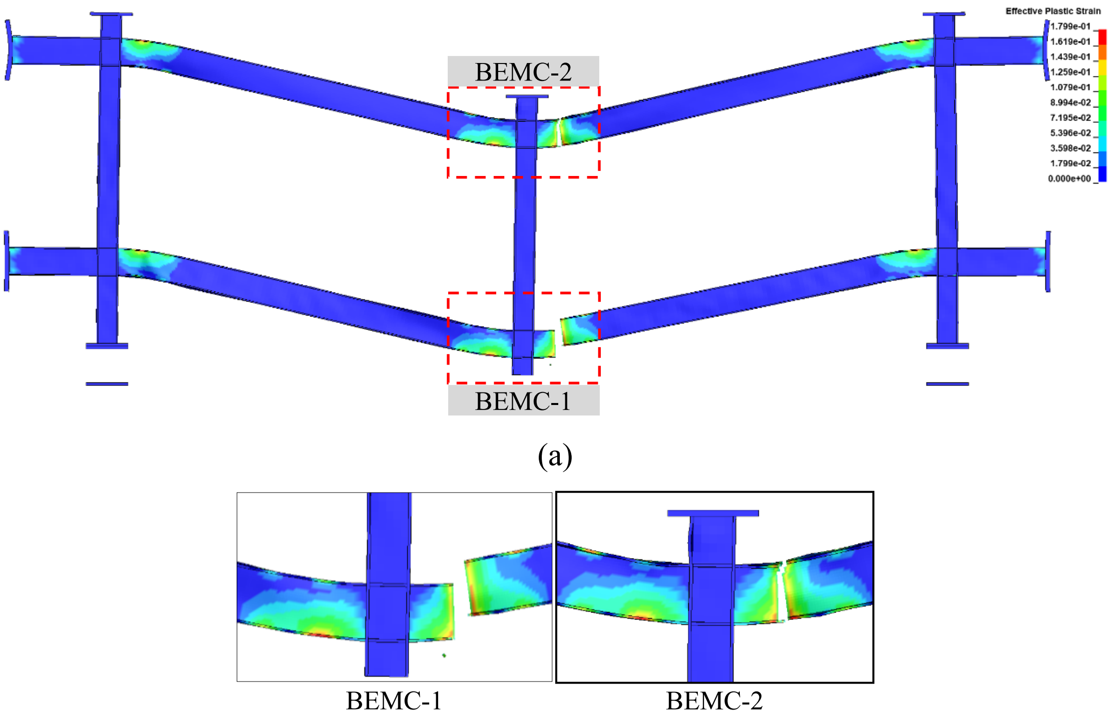

(a)

(b)

Fig. 27 Failure mode of DRBS: (a) overall view; (b) zone-in view

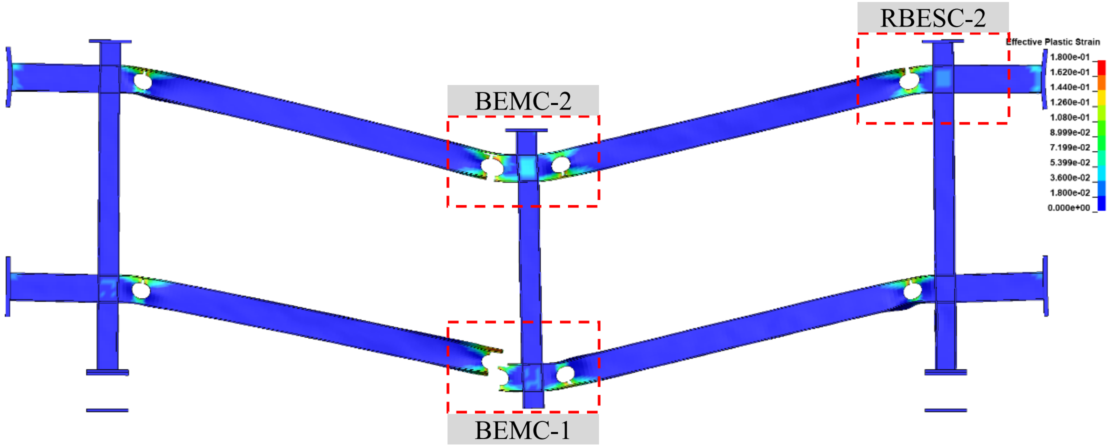

(a)

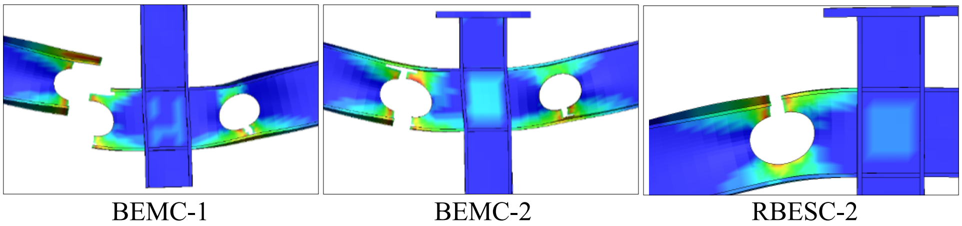

(b)

Fig. 28 Failure mode of OBW: (a) overall view; (b) zone-in view

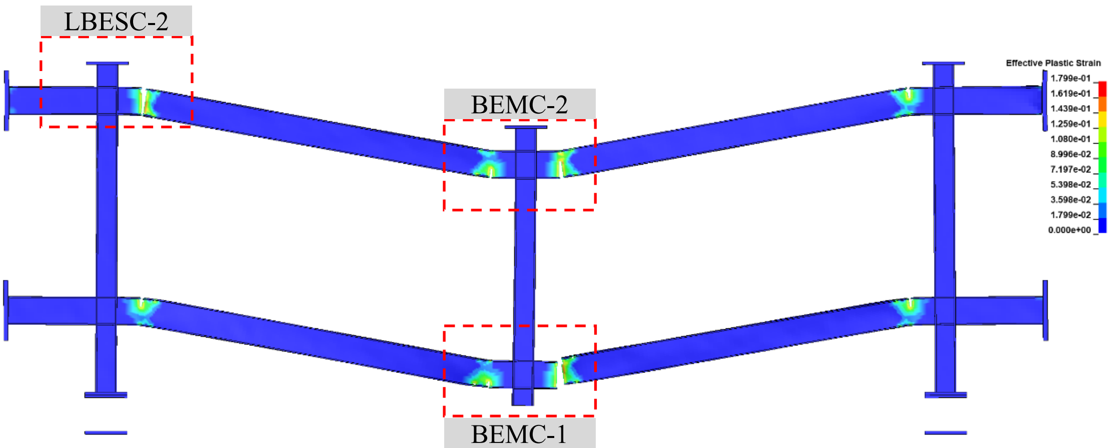

(a)

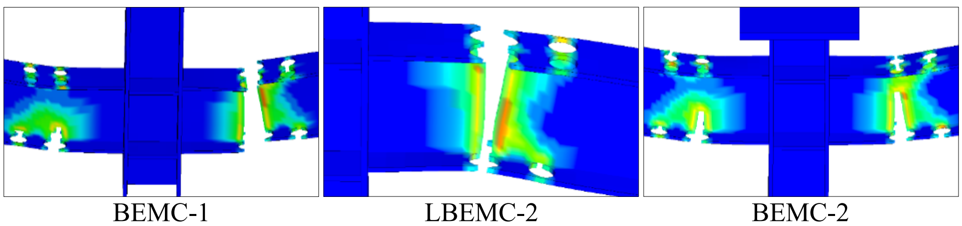

(b)

Fig. 29 Failure mode of OBF-2: (a) overall view; (b) zone-in view

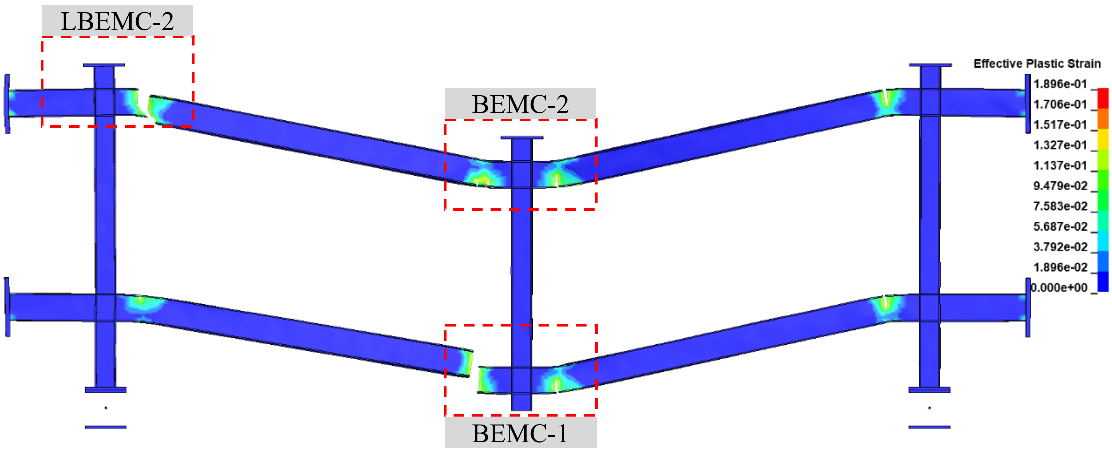

(a)

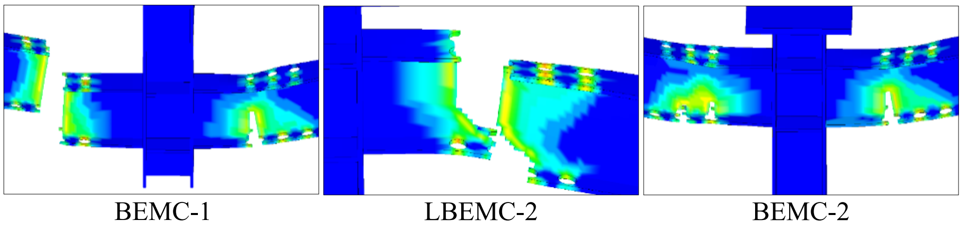

(b)

Fig. 30 Failure mode of OBF-3: (a) overall view; (b) zone-in view